Shape-imposed anisotropy in antiferromagnetic complex oxide nanostructures

A.D. Bang*[1], I. Hallsteinsen[1, 2], R.V. Chopdekar[2], F.K. Olsen[1], S.D. Slöetjes[1], K. Kjærnes[1], E. Arenholz[2], E. Folven[1], J.K. Grepstad[1]

[1] *Department of Electronic Systems, Norwegian University of Science and Technology (NTNU), Trondheim 7491, Norway*

[2]*Advanced Light Source, Lawrence Berkeley National Laboratory, Berkeley, CA 94720, USA*

In this study, we report on a shape-imposed magnetic anisotropy in micro- and nanostructures defined in antiferromagnetic (AF) $LaFeO_3$ (LFO) thin films. Two distinct types of structures are investigated; embedded magnets created via ion implantation, and free-standing magnets created via ion milling. Using a combination of x-ray photoemission electron microscopy and x-ray absorption spectroscopy, we examine the impact of structure type, AF layer thickness, and crystal geometry on the Néel vector orientation in these structures. We demonstrate a distinct shape-imposed anisotropy in embedded and free-standing structures alike, and show that both parallel and perpendicular alignment of the AF spin axis with respect to structure edges can be achieved by variation of the AF layer thickness and the orientation of the structure edges with respect to the LFO crystalline axes. This work demonstrates how fabrication procedure affects the magnetic order in thin film AF nanostructures and shows how nanoscale patterning can be used to control the orientation of the Néel vector in epitaxial oxide thin films.

*ambjorn.bang@ntnu.no

Antiferromagnetic (AF) devices have recently emerged as a promising prospect in the field of spintronics.[1-6] Insensitive to magnetic interference and with ultrafast spin dynamics, these materials promise stable, high-speed devices with a higher packing density than analogous ferromagnetic (FM) devices. However, the magnetically compensated nature of AF ordering precludes conventional ways of magnetic spin control, necessitating new techniques for manipulation and read-out of the AF spin configuration.

The magnetic domain patterns observed in AF materials are commonly explained in terms of lattice imperfections, such as defects and structural domains.[7-13] In AF thin films, the orientation of the spin axis is highly sensitive to strain, thus allowing manipulation via epitaxial strain[14-16] or by growth on vicinal substrates.[17-19] Moreover, in the absence of long-range magnetostatic forces, theoretical studies suggest that magnetoelastic forces in combination with surface anisotropy can lead to shape effects in the AF domain pattern.[20,21] Experimental studies of such AF shape effects are scarce, however, due to the challenges associated with patterning and magnetic measurements of AF structures with appropriate dimensions.

We have previously demonstrated shape effects in the AF domain pattern of $LaFeO_3$ (LFO) thin film nanomagnets with edges aligned along the reported magnetocrystalline easy axes of LFO.[22,23] Combined with FM $La_{0.7}Sr_{0.3}MnO_3$ (LSMO) in an AF/FM bilayer, this shape-imposed anisotropy was shown to affect both the domain pattern and the switching characteristics of the adjacent FM layer.[24-29]

In the present study, we investigate the effects of layer thickness, crystalline orientation, and fabrication procedure (i.e., embedded vs. free-standing structures) on the shape-imposed magnetic domain pattern in LFO thin film micro- and nanostructures. Using a combination of x-ray photoemission electron microscopy (X-PEEM) and x-ray absorption spectroscopy (XAS), the orientation of the Néel vector was determined from magnetic linear dichroism in the x-ray absorption. In embedded and free-standing magnets alike, we observe a pronounced reorientation of the AF spin axis near the nanomagnet edges, implying the presence of a shape-imposed anisotropy. Moreover, the favored axis for this shape-imposed anisotropy is found to depend on structure type (embedded vs. free-standing), layer thickness, and crystalline orientation of the nanomagnet edges.

LFO thin films were grown epitaxially on (001)-oriented, Nb-doped (0.05 wt %) $SrTiO_3$ (STO) substrates using growth parameters stated in previous reports.[22,23] The

*ambjorn.bang@ntnu.no

STO(001) substrates were miscut at an 0.1˚ angle, and feature a step-and-terrace surface morphology. The layer thicknesses were 60, 45 and 10 u.c. thick (1 u.c. ≈ 0.4 nm). Electron beam lithography was used to define micro- and nanostructures in a resist layer (CSAR62), creating a resist mask. Two different techniques were used to transfer the patterns to the underlying thin film. Embedded nanomagnets were prepared using a previously reported technique relying on Ar^+ ion implantation.[22,30] The implanted Ar^+ ions disrupt the LFO crystalline lattice, effectively suppressing the magnetic order outside of masked regions without removing material. The ion implantation also causes implanted regions to swell by 2–10 nm dependent on film thickness. Free-standing structures were made using chemically assisted ion beam etching (CAIBE) with a mixture of Ar^+ ions and O_2. The fabrication processes, including post-processing characterization, are described in further detail in the Supplementary information.

X-ray absorption measurements with linearly polarized x-rays were carried out at the Advanced Light Source (ALS). Two complementary measurement techniques were used, X-PEEM at the PEEM3 endstation (beamline 11.0.1) and XAS at the Magnetic Spectroscopy and Scattering beamline 4.0.2. The X-PEEM images were recorded with the incident x-rays at 30˚ (grazing) incidence, and magnetic contrast for AF domains of different spin axis orientation was obtained from x-ray magnetic linear dichroism (XMLD) in the absorption of s-polarized x-rays tuned to the two maxima of the Fe L_2 multiplet. On beamline 4.0.2, XMLD spectra characteristic of different AF spin configurations were obtained from the Fe $L_{2,3}$ absorption spectrum, measured via the sample drain current (total electron yield), with the linearly polarized x-rays incident normal to the sample surface (see inset in Fig.2a).

Figure 1 shows X-PEEM images of free-standing line structures in a 60 u.c. LFO film (a-c) and embedded line structures in a 10 u.c. film (d-f), recorded at room temperature (T = 300 K). The ”square wave” line structures have linewidths of 1 μm, 500 nm, and 250 nm, respectively, and the line edges are aligned with in-plane pseudo-cubic <100> directions. A pronounced shape effect leading to formation of extended domains at the edges is found for all linewidths. We note that the domain contrast is reversed for the two samples. In the 60 u.c. free-standing line structures (figure 1a-c), the observed contrast indicates a parallel alignment of the Néel vector with respect to the structure edges. The opposite XMLD contrast, recorded for the 10 u.c. embedded structures (figure 1 d-f), implies the AF spin axis to be aligned perpendicular to the structure edges. The lateral width of these “edge domains” appears to be similar, irrespective of the difference in layer thickness (10 vs. 60 u.c.) and structure type

*ambjorn.bang@ntnu.no

(embedded vs. free-standing). For the 1 µm wide lines, shown in figures 1a and 1d, the "edge domains" extend inwards ~200 nm, beyond which the domain pattern resembles the multi-domain pattern commonly reported for LFO blanket films.[7,19,23,31] When the linewidth is reduced below the combined widths of two opposite "edge domains", the two domains coalesce, as seen in figures 1b,c and 1e,f.

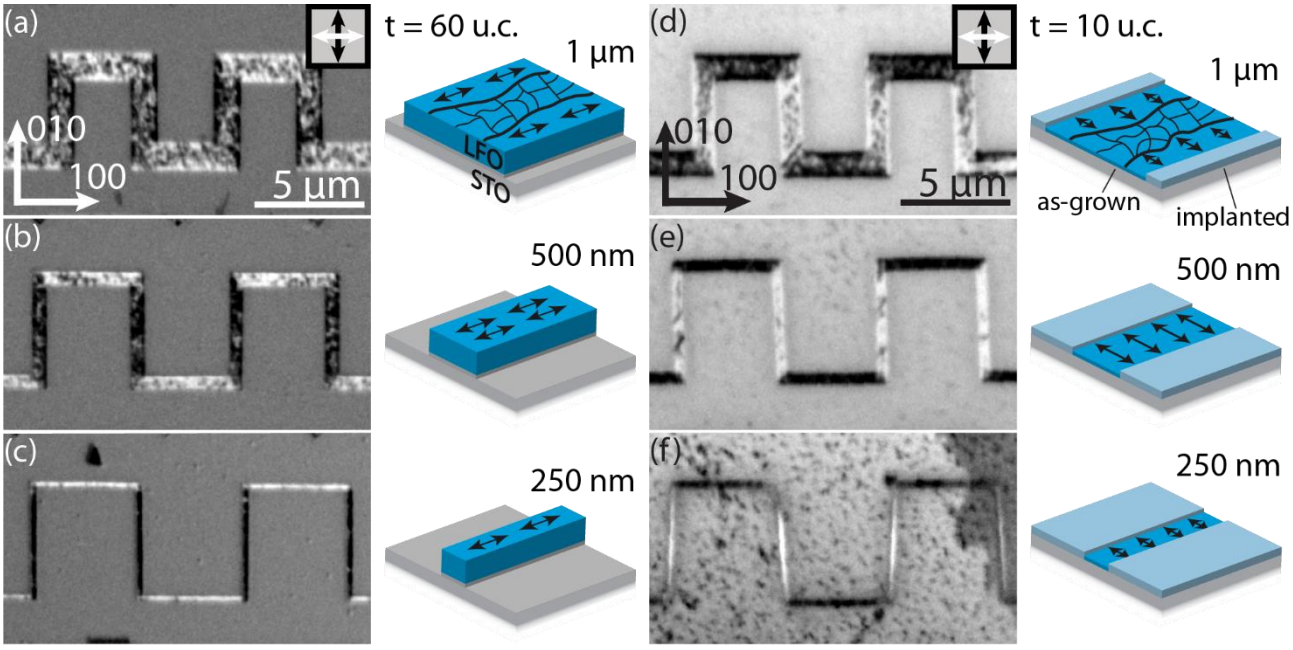

Figure 1: X-PEEM images comparing thick (60 u.c.) free-standing and thin (10 u.c.) embedded nanostructures. (a-f) show «square wave» line structures of linewidth 1 µm, 500 nm, and 250 nm, respectively. Legends in the top images (a) and (d) apply to all images. The schematics depict the topographic shape and predominant AF spin axes orientation for these line structures, and emphasize the linewidth dependence of the domain patterns and the difference in spin axis orientation for free-standing and embedded structures.

In AF thin film epilayers, the XMLD spectral signature is known to depend on the angle between the AF spin axis and the *E*-vector of the linearly polarized x-rays, as well as their orientation with respect to the crystalline axes.[32-35] A careful consideration of the experimental geometry is therefore imperative to a correct interpretation of the XMLD spectra concerning the orientation of the AF spin axis.[33] The XMLD signature of the Fe $L_{2,3}$ absorption edge in an octahedral crystal field is predicted to change sign dependent on whether the AF spin axis is aligned along the <100> or the <110> crystalline direction.[34] This sign reversal was experimentally verified by Arenholz et al. for an LSMO/$La_{0.7}Sr_{0.3}FeO_3$ (LSFO) $[6 \text{ u.c.} \times 6 \text{ u.c.}]_{10}$ superlattice.[36] In order to verify a corresponding sign reversal in our LFO thin films, we investigated the impact of the film crystalline orientation by taking

*ambjorn.bang@ntnu.no

advantage of the interface exchange coupling in an LFO/LSMO bilayer.[24,25] The vector magnet on beamline 4.0.2 was used to align the Néel vector in the AF LFO layer via the interface coupling to FM moments in the LSMO layer, thereby allowing measurements with the Néel vector oriented along different crystalline axes.

Figure 2 presents XAS-XMLD measurements of a 10/90 u.c. LFO/LSMO bilayer film, recorded at T = 80 K. The experimental setup is shown in the inset of figure 2a. The XMLD difference spectra were obtained by subtracting the spectra recorded in normal incidence with the *E*-vector aligned along ω = 0˚ and ω = 90˚, respectively. A magnetic field of 0.3 T was applied either parallel (H_y) or perpendicular (H_x) to the ω = 0˚ polarization. The field is canted 20˚ out of the film plane, so as to prevent trapping of low-energy emitted electrons, thus increasing the total electron yield. The magnetic dichroism measured at the Mn $L_{2,3}$-edge (not shown) confirmed that the FM moments in LSMO were aligned with the in-plane projection of the applied magnetic field. Moreover, a rotatable sample holder allows the ω = 0˚ and ω = 90˚ polarizations to be aligned with different in-plane crystalline directions. Two different measurement geometries were explored; (i) *E*-vector parallel and perpendicular to an in-plane $<100>_{pc}$ axis and (ii) *E*-vector parallel and perpendicular to an in-plane $<110>_{pc}$ axis, in the following referred to as the $<100>_{pc}$ and $<110>_{pc}$ geometry, respectively. Figure 2a shows the x-ray absorption spectra for ω = 0˚ and 90˚ and the XMLD difference spectrum, recorded for the $<100>_{pc}$ geometry with the applied field in the x-direction (H_x). Based on the interpretation established by Arenholz et al,[38] the measured XMLD spectrum implies that the AF spin axis is oriented perpendicular to the applied field H_x and the FM moments of LSMO, in keeping with the previously reported (spin-flop) interface coupling in this materials system.[24,25]

*ambjorn.bang@ntnu.no

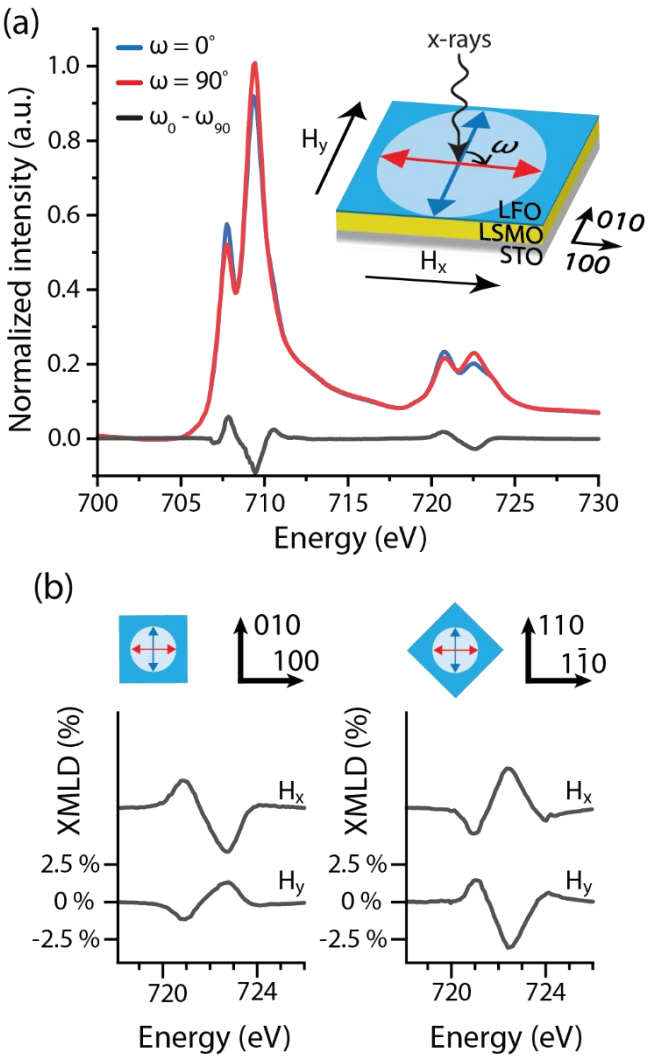

Figure 2: XAS-XMLD measurements in an applied magnetic field for a 10/90 u.c. LFO/LSMO blanket film at T = 80 K. (a) Fe $L_{2,3}$ absorption spectra and corresponding XMLD difference spectrum recorded in <100> geometry with an applied field in the x-direction (H_x). The experimental setup is depicted in the inset. The blue (red) arrow designates the polarization plane for ω = 0 °(ω = 90°). (b) XMLD spectra recorded at the L_2-edge for two orthogonal directions of the applied field, measured in two different geometries, $<100>_{pc}$ and $<110>_{pc}$, as indicated by the legends on top.

Figure 2b presents the XMLD difference spectra for the Fe L_2-edge in both geometries ($<100>_{pc}$ and $<110>_{pc}$) and two orthogonal directions of the applied field (H_x and H_y). Comparing the in-field XMLD spectra, we note the difference in spectral signature for orthogonal directions of the applied field, inverted between the $<100>_{pc}$ and $<110>_{pc}$ geometries. As the AF spin axis orientation is governed by the interface coupling to the adjacent FM layer, the magnetization of which is controlled by the applied field, this

*ambjorn.bang@ntnu.no

observation clearly shows that the XMLD signature changes sign when the Néel vector is reoriented from a $<100>_{pc}$ to a $<110>_{pc}$ direction, corroborating the previously reported multiplet calculations for Fe.[31,34]

In order to explore the impact of film crystalline orientation, layer thickness, and type of structure (embedded vs. free-standing) on the AF shape effect, XAS-XMLD spectra were measured for a series of patterned LFO thin films. Extended arrays (2.5 x 2.5 mm^2) of straight lines were defined in these films, so as to ensure a complete overlap with the full spot of the x-ray beam (~100 x 100 μm^2). A linewidth of 500 nm was chosen for these measurements, as this appears to be the maximum linewidth for which the domain pattern is entirely composed of shape-imposed «edge domains» (cf. Fig. 1b and e). All spectra were recorded in normal incidence with the *E*-vector of the linearly polarized x-rays parallel ($\omega = 0^\circ$) or perpendicular ($\omega = 90^\circ$) to the lines, as indicated in the inset of figure 3a. The line arrays were defined in films of two different layer thicknesses (10 u.c. and 45 u.c.) with the lines parallel to in-plane $<100>_{pc}$ and $<110>_{pc}$ crystalline axes, respectively, for both embedded and free-standing structures. In total, 8 unique line-patterned samples were measured. Figure 3a presents the x-ray absorption spectra with the corresponding XMLD difference spectrum recorded for free-standing lines aligned with a $<100>_{pc}$ crystalline axis, defined in a 45 u.c. LFO thin film. Given the $<100>_{pc}$ measurement geometry, the observed dichroism suggests an AF spin axis parallel to the lines. We have previously demonstrated that an unpatterned (blanket) film measured in a similar setup yields no net dichroism signal, proving that the dichroism observed in the present sample arises due to the line-patterning.[29]

*ambjorn.bang@ntnu.no

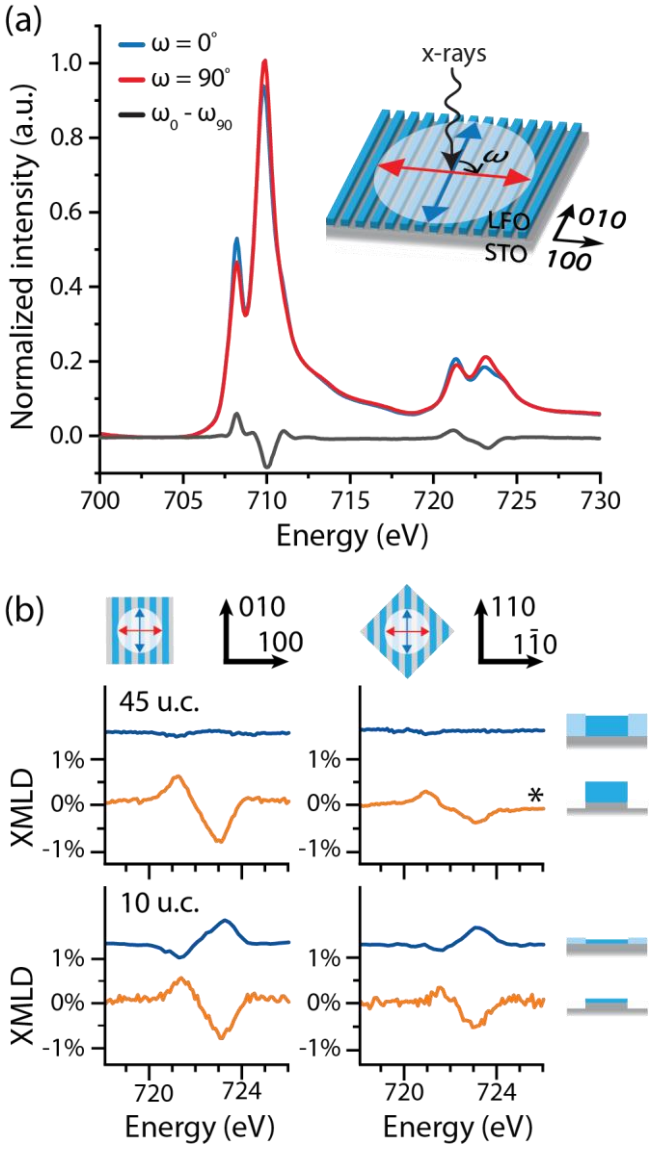

Figure 3: XAS-XMLD measurements for extended line arrays of 500 nm wide lines patterned in LFO thin films. (a) Fe $L_{2,3}$ absorption spectra and corresponding XMLD difference spectrum measured for <100>$_{pc}$-oriented free-standing lines in a 45 u.c. LFO film at T = 80 K. The experimental setup is depicted in the inset. The blue (red) arrow designates the polarization plane for ω = 0° (ω = 90°). (b) XMLD spectra recorded at the L_2-edge for the patterned films at T = 300 K, (except for the spectrum marked by an asterisk, for which T = 80 K). The two columns of XMLD difference spectra are measured for line arrays oriented along <100>$_{pc}$ and <110>$_{pc}$ crystalline directions, respectively, as indicated by the legends on top. The top (bottom) set of spectra correspond to nanomagnets patterned in a 45 u.c. (10 u.c.) film, whereas their color indicates the structure type, blue for embedded structures and orange for free-standing structures.

Figure 3b compares XMLD spectra measured at the Fe L_2-edge for these 8 unique line patterns. In the 45 u.c LFO layer, no linear dichroism was observed for embedded line structures in either of the two crystalline orientations (<100>$_{pc}$ and <110>$_{pc}$), precluding a preferential Néel vector orientation in these structures. For the other line patterns, we note the absence of sign reversal in the XMLD spectra between the <100>$_{pc}$ and <110>$_{pc}$ orientations. On account of the established sign reversal for the XMLD difference spectrum for different

*ambjorn.bang@ntnu.no

in-plane crystalline orientations of the AF spin axis in blanket films (cf. the analysis of figure 2 above), this finding implies that the favored Néel vector orientation changes depending on the crystalline orientation of the line edges. A schematic summarizing the Néel vector alignment for the 8 different LFO line patterns is shown in figure 4. For free-standing line structures defined in a 45 u.c. film, the XMLD spectrum suggests that the Néel vector is oriented parallel to the edges for $<100>_{pc}$-oriented lines (parallel spin alignment), whereas the Néel vector is aligned perpendicular to the edges for $<110>_{pc}$-oriented lines (perpendicular spin alignment). We note that the XMLD spectrum for the latter geometry in figure 3 was obtained at a temperature of T = 80 K. The amplitude of this XMLD spectrum is considerably reduced compared to that measured for $<100>_{pc}$-oriented lines at the same temperature (~20 % of the amplitude for the XMLD spectrum recorded at T = 80 K, not shown), suggesting that perpendicular alignment of the AF spins is less predominant for this geometry, i.e. domains with different spin axis orientations are still present. In the 10 u.c. films, a distinct linear dichroism is observed for all four line patterns. For embedded lines, the dichroism signature indicates perpendicular spin alignment for $<100>_{pc}$-oriented lines and parallel spin alignment for $<110>_{pc}$-oriented lines. In free-standing line structures, the situation is reversed. Here, parallel spin alignment is found in $<100>_{pc}$-oriented lines, whereas $<110>_{pc}$-oriented lines exhibit perpendicular spin alignment.

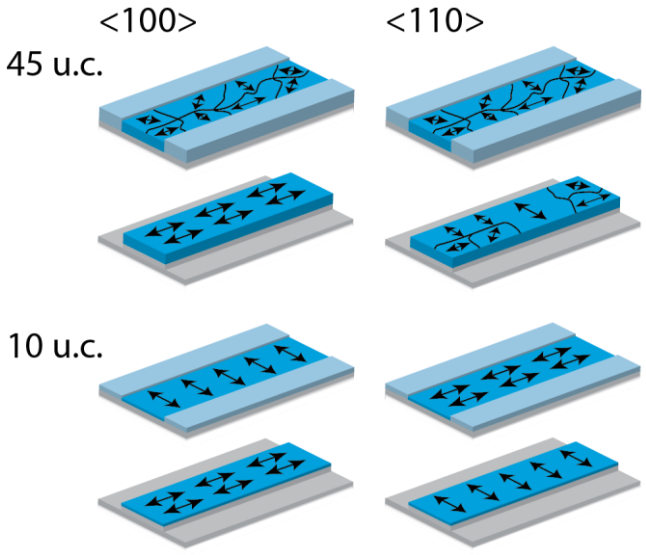

Figure 4: Schematic summary of the AF spin axis orientations for the LFO thin film nanostructures investigated.

*ambjorn.bang@ntnu.no

The shape-imposed AF spin anisotropy reported in this study is found to depend on film thickness and crystalline orientation, as well as on whether the structures are embedded or free-standing. The orientation of the AF spin axis in LFO thin films is known to be highly sensitive to minute changes in the crystal structure, as demonstrated by the variation in out-of-plane canting reported for different growth conditions on STO(001),[7,19,22,31] the impact of structural domains,[37,38] thermal relaxation,[22,39] and variations with film thickness.[40] The fabrication of embedded as well as free-standing structures implies a strain modulation near the structure edges. X-ray diffraction analysis of embedded LSMO nanostructures patterned using the same techniques, showed a compressive strain on the nanostructures imposed by the embedding matrix.[41] Moreover, Gomonay et al.[20,21] have proposed a model, taking into account both surface magnetic anisotropy and long-range magnetoelastic forces, which predicts a shape-dependent magnetic anisotropy for AF nanoparticles consistent with our findings. We thus contend that the observed shape-imposed anisotropy results from a strain-induced modulation of the crystal structure near the edges affecting the local magnetocrystalline anisotropy. The different results recorded for 10 u.c. and 45 u.c. layers are tentatively attributed to thickness variations in the magnetocrystalline anisotropy.[23]

We note that no shape effect was observed in embedded lines oriented along a $<100>_{pc}$ direction in the 45 u.c. layer, despite this being a magnetocrystalline easy axis for LFO. The $<100>_{pc}$-oriented embedded lines in the thinner 10 u.c. layer showed perpendicular spin alignment, whereas we have previously reported parallel spin alignment for embedded $<100>_{pc}$-oriented structures in a 100 u.c. layer.[22] A possible explanation for the apparent absence of shape effects in the 45 u.c. layer could thus be that this layer thickness represents a transition regime for which perpendicular and parallel spin alignment is equally favored, thus promoting a frustrated AF domain state.

In conclusion, we demonstrate a pronounced shape-induced anisotropy in the AF domain pattern of micro- and nanostructures prepared using ion implantation (embedded structures) or ion milling (free-standing structures) in LFO thin films. Extended domains with a width of ~200 nm were observed along the edges of line structures aligned with the magnetocrystalline easy axes of LFO thin film epilayers. By reducing the linewidth to $\leq$ 500 nm, the domain pattern is dominated by this shape-imposed anisotropy. Furthermore, we have demonstrated how the preferred orientation of the AF spin axis (parallel/perpendicular) depends critically on the AF layer thickness and crystalline orientation of the lines, as well as on the fabrication procedure (embedded vs. free-standing structures). We attribute this finding

*ambjorn.bang@ntnu.no

to a local modulation of strain from the patterning procedure, combined with a thickness-dependent magnetocrystalline anisotropy. This study demonstrates how the AF spin configuration can be manipulated by nanostructuring, thus offering a possibility for Néel vector control in novel devices.

Supplementary Material

See supplementary material for an overview of the two fabrication processes used to create embedded and free-standing structures, as well as atomic force microscopy images of the processed samples.

Acknowledgments

This research was undertaken with funding from the Research Council of Norway, under grant no. 231290. Partial funding was also obtained from the Norwegian PhD Network on Nanotechnology for Microsystems (A.D.B.), which is sponsored by the Research Council of Norway, Division for Science, under contract no. 221860/F60. The Advanced Light Source is supported by the Director, Office of Science, Office of Basic Energy Sciences, and the U.S. Department of Energy under contract DE-AC02-05CH11231. Nanoscale patterning was carried at NTNU NanoLab, NorFab. The Research Council of Norway is acknowledged for the support to the Norwegian Micro- and Nanofabrication Facility, NorFab, project number 245963/F50

[1] E. V. Gomonay and V. M. Loktev, Low Temperature Physics **40** (1), 17 (2014).
[2] T. Jungwirth, J. Sinova, A. Manchon, X. Marti, J. Wunderlich, and C. Felser, Nature Physics **14** (3), 200 (2018).
[3] T. Jungwirth, X. Marti, P. Wadley, and J. Wunderlich, Nature Nanotechnology **11** (3), 231 (2016).
[4] O. Gomonay, V. Baltz, A. Brataas, and Y. Tserkovnyak, Nature Physics **14** (3), 213 (2018).
[5] J. Železný, P. Wadley, K. Olejník, A. Hoffmann, and H. Ohno, Nature Physics **14** (3), 220 (2018).
[6] K. Olejník, V. Schuler, X. Marti, V. Novák, Z. Kašpar, P. Wadley, R. P. Campion, K. W. Edmonds, B. L. Gallagher, J. Garces, M. Baumgartner, P. Gambardella, and T. Jungwirth, Nature Communications **8**, 15434 (2017).

*ambjorn.bang@ntnu.no

[7] A. Scholl, J. Stöhr, J. Lüning, J. W. Seo, J. Fompeyrine, H. Siegwart, J.-P. Locquet, F. Nolting, S. Anders, E. E. Fullerton, M. R. Scheinfein, and H. A. Padmore, Science **287** (5455), 1014 (2000).

[8] J. W. Seo, E. E. Fullerton, F. Nolting, A. Scholl, J. Fompeyrine, and J. P. Locquet, Journal of Physics: Condensed Matter **20** (26), 264014 (2008).

[9] Y. Y. Li, Physical Review **101** (5), 1450 (1956).

[10] J. Baruchel, M. Schlenker, and W. L. Roth, Journal of Applied Physics **48** (1), 5 (1977).

[11] M. K. Wilkinson, J. W. Cable, E. O. Wollan, and W. C. Koehler, Physical Review **113** (2), 497 (1959).

[12] S. B. Palmer, Journal of Physics F, Metal Physics **5** (12), 2370 (1975).

[13] J. Stöhr, A. Scholl, T. J. Regan, S. Anders, J. Lüning, M. R. Scheinfein, H. A. Padmore, and R. L. White, Physical Review Letters **83** (9), 1862 (1999).

[14] J. Zhu, Q. Li, J. X. Li, Z. Ding, C. Y. Hua, M. J. Huang, H. J. Lin, Z. Hu, C. Won, and Y. Z. Wu, Journal of Applied Physics **115** (19), 193903 (2014).

[15] J. Li, E. Arenholz, Y. Meng, A. Tan, J. Park, E. Jin, H. Son, J. Wu, C. A. Jenkins, A. Scholl, H. W. Zhao, C. Hwang, and Z. Q. Qiu, Physical Review B **84** (1), 012406 (2011).

[16] W. Kim, E. Jin, J. Wu, J. Park, E. Arenholz, A. Scholl, C. Hwang, and Z. Q. Qiu, Physical Review B **81** (17), 174416 (2010).

[17] Y. Z. Wu, Z. Q. Qiu, Y. Zhao, A. T. Young, E. Arenholz, and B. Sinkovic, Physical Review B **74** (21), 212402 (2006).

[18] Q. Li, T. Gu, J. Zhu, Z. Ding, J. X. Li, J. H. Liang, Y. M. Luo, Z. Hu, C. Y. Hua, H. J. Lin, T. W. Pi, C. Won, and Y. Z. Wu, Physical Review B **91** (10), 104424 (2015).

[19] J. Lüning, F. Nolting, A. Scholl, H. Ohldag, J. W. Seo, J. Fompeyrine, J. P. Locquet, and J. Stöhr, Physical Review B **67** (21), 214433 (2003).

[20] H. V. Gomonay and V. M. Loktev, Physical Review B **75** (17), 174439 (2007).

[21] O. Gomonay, S. Kondovych, and V. Loktev, Journal of Magnetism and Magnetic Materials **354**, 125 (2014).

[22] E. Folven, T. Tybell, A. Scholl, A. Young, S. T. Retterer, Y. Takamura, and J. K. Grepstad, Nano Letters **10** (11), 4578 (2010).

[23] E. Folven, A. Scholl, A. Young, S. T. Retterer, J. E. Boschker, T. Tybell, Y. Takamura, and J. K. Grepstad, Physical Review B **84** (22), 220410 (2011).

[24] Y. Takamura, E. Folven, J. B. R. Shu, K. R. Lukes, B. Li, A. Scholl, A. T. Young, S. T. Retterer, T. Tybell, and J. K. Grepstad, Physical Review Letters **111** (10) (2013).

[25] E. Folven, A. Scholl, A. Young, S. T. Retterer, J. E. Boschker, T. Tybell, Y. Takamura, and J. K. Grepstad, Nano Letters **12** (5), 2386 (2012).

[26] E. Folven, J. Linder, O. V. Gomonay, A. Scholl, A. Doran, A. T. Young, S. T. Retterer, V. K. Malik, T. Tybell, Y. Takamura, and J. K. Grepstad, Physical Review B **92** (9), 094421 (2015).

[27] M. S. Lee, T. A. Wynn, E. Folven, R. V. Chopdekar, A. Scholl, S. T. Retterer, J. K. Grepstad, and Y. Takamura, Physical Review Materials **1** (1), 014402 (2017).

[28] A. D. Bang, F. K. Olsen, S. D. Slöetjes, A. Scholl, S. T. Retterer, C. A. F. Vaz, T. Tybell, E. Folven, and J. K. Grepstad, Applied Physics Letters **113** (13), 132402 (2018).

[29] A. D. Bang, I. Hallsteinsen, F. K. Olsen, S. D. Slöetjes, S. T. Retterer, A. Scholl, E. Arenholz, E. Folven, and J. K. Grepstad, Applied Physics Letters **114** (19), 192403 (2019).

[30] Y. Takamura, R. V. Chopdekar, A. Scholl, A. Doran, J. A. Liddle, B. Harteneck, and Y. Suzuki, Nano Letters **6** (6), 1287 (2006).

[31] S. Czekaj, F. Nolting, L. J. Heyderman, P. R. Willmott, and G. van der Laan, Physical Review B **73** (2), 020401 (2006).

[32] G. van der Laan, E. Arenholz, R. V. Chopdekar, and Y. Suzuki, Physical Review B **77** (6), 064407 (2008).

[33] E. Arenholz, G. van der Laan, and F. Nolting, Applied Physics Letters **93** (16), 162506 (2008).

[34] E. Arenholz, G. van der Laan, R. V. Chopdekar, and Y. Suzuki, Physical Review B **74** (9), 094407 (2006).

*ambjorn.bang@ntnu.no

[35] E. Arenholz, G. van der Laan, R. V. Chopdekar, and Y. Suzuki, Physical Review Letters **98** (19), 197201 (2007).
[36] E. Arenholz, G. van der Laan, F. Yang, N. Kemik, M. D. Biegalski, H. M. Christen, and Y. Takamura, Applied Physics Letters **94** (7), 072503 (2009).
[37] S. Czekaj, F. Nolting, L. J. Heyderman, K. Kunze, and M. Krüger, Journal of Physics: Condensed Matter **19** (38), 386214 (2007).
[38] I. Hallsteinsen, M. Moreau, R. V. Chopdekar, E. Christiansen, M. Nord, P. E. Vullum, J. K. Grepstad, R. Holmestad, S. M. Selbach, A. Scholl, E. Arenholz, E. Folven, and T. Tybell, APL Materials **5** (8), 086107 (2017).
[39] J. K. Grepstad, Y. Takamura, A. Scholl, I. Hole, Y. Suzuki, and T. Tybell, Thin Solid Films **486** (1), 108 (2005).
[40] I. Hallsteinsen, A. Grutter, M. Moreau, S. D. Slöetjes, K. Kjærnes, E. Arenholz, and T. Tybell, Physical Review Materials **2** (8), 084403 (2018).
[41] F. K. Olsen, unpublished (2019).

*ambjorn.bang@ntnu.no

Supplementary Information for:

Shape-imposed anisotropy in antiferromagnetic complex oxide nanostructures

A.D. Bang[1], I. Hallsteinsen[1, 2], R.V. Chopdekar[2], F.K. Olsen[1], S.D. Slöetjes[1] K. Kjærnes[1], E. Arenholz[2], E. Folven[1], J.K. Grepstad[1]

[1] *Department of Electronic Systems, Norwegian University of Science and Technology (NTNU), Trondheim 7491, Norway*
[2]*Advanced Light Source, Lawrence Berkeley National Laboratory, Berkeley, CA 94720, USA*

LFO thin film patterning process

The patterning process for free-standing and embedded structures are summarized in the schematic shown in figure S1a below. A resist layer of ~ 430 nm CSAR62 was applied on the thin film samples by spin coating. The line structures were then defined using standard electron beam lithography processing.

To create embedded structures, the masked samples were exposed to a bombardment of Ar^+ ions accelerated to ~50 keV. In this energy range, the Ar^+ ions penetrate the entire film thickness where unprotected, degrading crystalline order and rendering the exposed film paramagnetic.[1] Finally, the mask is removed, leaving an array of AF line structures embedded in an implanted paramagnetic matrix.

To create free-standing structures, ion milling with chemically assisted ion beam etching (CAIBE) was used. The samples were etched using a mixture of Ar and O_2 in order to prevent resist hardening. Using Ar and O_2 in a 1/5 ratio, a 10 nm/min etching rate for LFO was achieved, with a 1:3 selectivity to the resist mask. To ensure the removal of all magnetic material outside of the masked area, an etching depth of 50 nm was used, etching well into the

$SrTiO_3$ substrate. Subsequent removal of the remaining resist mask completes the processing of samples with freestanding structures.

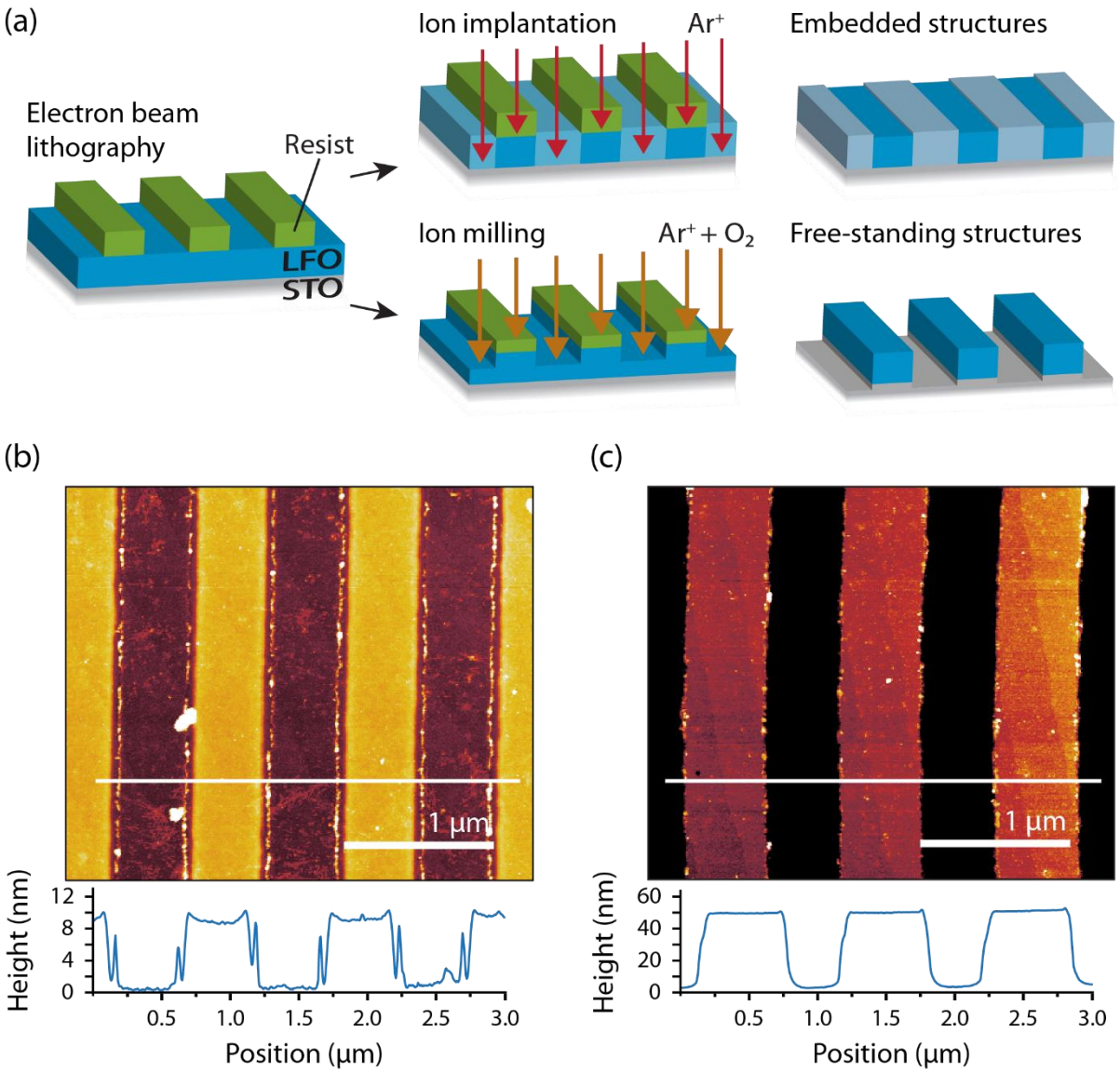

Figure S1: (a) Schematic summary of the patterning process for embedded and free-standing structures in LFO thin films. (b)-(c) AFM image and height profiles measured for embedded (b) and free-standing (c) structures in a 45 u.c. LFO layer. The height profiles are measured along the white lines in the AFM images.

Post-patterning characterization:

Figure S1b-c present AFM images with height profiles of embedded and free-standing line structures measured after completion of the patterning process. Crystalline nanomagnet surfaces with unit cell height step-edge morphology are preserved after all processing steps for both fabrication procedures. Minor residues from the resist mask were observed on all

samples. In the embedded structures, such residue is prominent in a thin zone along the edges. These residues presumably arise from resist hardening associated with Ar^+ ions impinging on the mask walls during bombardment. (The ion beam is slanted 7˚ w.r.t. normal incidence in combination with sample rotation, so as to prevent shadowing and ion channeling effects). The implanted matrix in samples with embedded structures is observed to swell by ~10 nm for the 45 u.c. layer (figure S1b), and ~ 2 nm for the 10 u.c. layer (not shown).

[1] E. Folven, T. Tybell, A. Scholl, A. Young, S. T. Retterer, Y. Takamura, and J. K. Grepstad, Nano Letters **10** (11), 4578 (2010).